

A high-order adaptive algorithm for multispecies gaseous flows on mapped domains

L.D. Owen*, S.M. Guzik, X. Gao

Department of Mechanical Engineering, Colorado State University, Fort Collins, CO 80523, USA



ARTICLE INFO

Article history:

Received 8 September 2017
 Revised 16 April 2018
 Accepted 7 May 2018
 Available online 8 May 2018

Keywords:

High-order finite-volume method
 Nonlinear PDEs
 Adaptive-mesh refinement
 Compressible multispecies flows

ABSTRACT

A fourth-order accurate finite-volume method is developed and verified for solving strongly nonlinear, time-dependent, compressible, thermally perfect, and multispecies gaseous flows on mapped grids that are adaptively refined in space and time. The algorithm introduces a new scheme for numerical flux calculations in order to cope with the nonlinear, spatially and temporally varying thermodynamic and transport properties of the gaseous mixture. The fourth-order numerical error convergence and solution accuracy are verified using Couette flow, species mass diffusion bubble, and vortex convection and diffusion problem. The thermally perfect, multispecies functionality is validated using a one-dimensional shock tube and two-dimensional shock box problem. Results are obtained for the Mach reflection problem where a strong shock propagates in the multispecies gaseous flow along a ramp and are compared to the solution of the shock propagation in a single species, calorically perfect, gaseous flow over the same ramp. The validated algorithm is then applied to simulate a relatively complex flow configuration to examine the secondary flow mixing due to the double air jets along with the main inlet where a premixed fuel mixture flows in. Future investigations will focus on three-dimensional configurations.

© 2018 Elsevier Ltd. All rights reserved.

1. Introduction

Fluid flows are generally governed by nonlinear partial differential equations (PDEs). Flows involving multispecies are seen in many practical applications, such as mixing devices in the chemical and biological engineering, thermal and non-thermal plasmas in the synthesis of advanced materials or surface modification of materials, and combustion devices for energy and power generation. Modeling and simulation of such nonlinear dynamical fluid systems can be numerically difficult and computationally expensive due to the nature of multi-physics and multi-scales. In particular, combustion, which is of interest to our future applications is complex and requires fine spatial and temporal resolutions to resolve the flame fronts over a long integration time in order to capture appropriate flame dynamics [1–13]. In the calculations of combustion, fundamental understanding of the nonlinear interactive physical processes that influence transport of species in the mixture and of the proper modeling of these processes are essential to evaluate the effectiveness of combustion simulations and the design of efficient numerical algorithms for combustion modeling. Therefore, the present work focuses on the development, verification, and validation of an efficient and effective numerical algorithm for solving

nonlinear multispecies mixing flows, and thus builds the algorithmic infrastructure for future applications to combustion problems.

During the past decades, numerous numerical methods have been developed for solving fluid flows involving multispecies. There are classes of segregated or coupled methods depending on the fashion how the governing PDEs are solved, steady or transient solvers depending on the physical states of interest, low-Mach numbers or high-speed flows depending on compressibility considerations, and laminar or turbulent flows depending on the intensity level of fluctuations. In addition, differences exist in the methods when discretizing the nonlinear PDEs on structured or unstructured grids, evolving the discretized equations in time explicitly or implicitly, and computing them on homogeneous or non-homogeneous parallel architectures. The volume of literature is large and it is nearly impossible to carry out an exhaustive discussion. Interested readers may get a flavor of the variation from a few references [14–17], but by no means is this comprehensive. Nevertheless, among the literature on CFD algorithms for multispecies flows, the hydrodynamics adaptive mesh refinement (AMR) simulation [18] and the parallel implicit AMR scheme [19] are two examples that are most relevant to the present work in terms of the use of the finite-volume method and structured AMR, in addition to the capability of complex geometry and parallel computing. The distinct features of the computational infrastructure that the present work is built upon include (1) fourth-order accuracy in

* Corresponding author.

E-mail address: landon.owen@colostate.edu (L.D. Owen).

both time and space, (2) AMR with sub-cycling, (3) mapped grids by generalized curvilinear coordinate transformation, and (4) new computer programming models. The focus of the present work is the development, verification, and validation of the high-order finite-volume method to solve thermally perfect gaseous multi-species flow on adaptive and mapped grids. Specifically, the goal is to apply the validated algorithm to investigate the numerical and physical modeling of the transport and mixing processes of multi-species gaseous flows for better prediction of the nonlinear physical phenomena in fluid engineering.

The rest of the paper is organized as follows. The mathematical modeling of the compressible multispecies flow on mapped grids is described in Section 2, along with the constitutive models for the thermodynamic and transport properties. Section 3 briefly reviews and discusses the fourth-order finite-volume method and the fourth-order stencils for spatial discretization. Section 4 verifies the fourth-order solution accuracy using three problems: Couette flow, species mass diffusion bubble, and two-dimensional vortex convection and diffusion. The thermally perfect, multispecies algorithm is validated using a one-dimensional shock tube and two-dimensional shock box problem. The freestream preservation is verified using a doubly periodic domain initialized with a uniform flow. Section 5 shows the numerical results for the multispecies Mach reflection shock ramp problem and the multispecies mixing in a relative realistic configuration due to secondary air jets. Section 6 concludes the findings of this study and recommends future follow-up work.

2. Mathematical modeling for compressible viscous multispecies flows

2.1. Governing equations for mapped domains by generalized curvilinear coordinate transformation

For compressible, multispecies flow, the conservation equations are augmented with a set of species transport equations. The equations are transformed between physical space, denoted as \vec{x} , and computational space, denoted as $\vec{\xi}$. The grid is assumed to remain constant in time. Define the metric Jacobian, J , and transformation grid metrics, N^T , as [20]

$$J \equiv \det(\vec{\nabla}_x \vec{x}), \quad N^T = J \vec{\nabla}_x \vec{\xi}, \quad N = J (\vec{\nabla}_x \vec{\xi})^T,$$

where the symbol, T, denotes transpose operation. The divergence of a vector field in physical space is transformed to computational space using the mathematical relation of

$$\vec{\nabla}_x \cdot \vec{u} = \frac{1}{J} \vec{\nabla}_\xi \cdot (N^T \vec{u}).$$

Using grid metrics to transform the system of governing equations for a compressible thermally perfect gaseous mixture on a mapped grid, including the continuity, momentum, energy, and a set of species transport equations, results in the following

$$\frac{\partial (J\rho)}{\partial t} + \vec{\nabla}_\xi \cdot (N^T \rho \vec{u}) = 0 \quad (1)$$

$$\frac{\partial (J\rho \vec{u})}{\partial t} + \vec{\nabla}_\xi \cdot (N^T (\rho \vec{u} \vec{u} + p \vec{I})) = \vec{\nabla}_\xi \cdot (N^T \vec{\tau}) + J\rho \vec{f} \quad (2)$$

$$\begin{aligned} \frac{\partial (J\rho e)}{\partial t} + \vec{\nabla}_\xi \cdot (N^T \rho \vec{u} (e + \frac{p}{\rho})) \\ = \vec{\nabla}_\xi \cdot (N^T (\vec{\tau} \cdot \vec{u})) - \vec{\nabla}_\xi \cdot (N^T \vec{Q}) + J\rho \vec{f} \cdot \vec{u} \end{aligned} \quad (3)$$

$$\frac{\partial (J\rho c_n)}{\partial t} + \vec{\nabla}_\xi \cdot (N^T \rho c_n \vec{u}) = -\vec{\nabla}_\xi \cdot (N^T \vec{J}_n), \quad n=1 \dots N_s \quad (4)$$

where ρ , \vec{u} , and p , are the mixture density, velocity, and pressure, respectively. The number of total species in the mixture is N_s .

The pressure of the gaseous mixture is given by the ideal gas law

$$p = \sum_{n=1}^{N_s} \rho c_n \frac{R_u}{M_n} T = \sum_{n=1}^{N_s} \rho c_n R_n T,$$

where $R_u = 8.314511$ J/mol is the universal gas constant, M_n is the molar mass of the n th species, $R_n = R_u/M_n$ is the gas constant of the n th species, c_n is the mass fraction of the n th species, and T is the mixture temperature. The identity tensor is denoted by \vec{I} and the total specific energy is $e = |\vec{u}|^2/2 + \sum_{n=1}^{N_s} c_n h_n - p/\rho$ where h_n is the specific absolute enthalpy for the n th species. The calculation of h_n will be further detailed in the next section. The body force, \vec{f} , is per unit volume acting on the gaseous mixture. The mapped stress tensor, $\vec{\tau}$, is defined by

$$\vec{\tau} = 2\mu \left(\vec{S} - \frac{1}{3} J^{-1} \vec{I} \vec{\nabla}_\xi \cdot (N^T \vec{u}) \right),$$

where μ is the molecular viscosity of the mixture and \vec{S} is the strain rate tensor, which is defined by

$$\vec{S} = \frac{1}{2} \left((\vec{\nabla}_\xi \vec{u}) \left(\frac{N^T}{J} \right) + \left((\vec{\nabla}_\xi \vec{u}) \left(\frac{N^T}{J} \right) \right)^T \right).$$

The mass diffusion is modeled using Fick's law,

$$\vec{J}_n = -\rho D_n \vec{\nabla}_\xi c_n,$$

where D_n is the mass diffusion coefficient of the n th species. The mapped molecular heat flux is modeled using Fourier's law,

$$\vec{Q} = - \left(\kappa \frac{N}{J} \vec{\nabla}_\xi T - \sum_{n=1}^{N_s} (h_n \vec{J}_n) \right),$$

where κ is the thermal conductivity of the mixture.

The molecular diffusivity can be obtained from a given Schmidt number, Sc, using the relation

$$D_n = \frac{\mu}{\rho Sc}, \quad (5)$$

or Lewis number, Le, using the relation

$$D_n = \frac{\kappa}{\rho c_p Le}. \quad (6)$$

We assume the mass diffusion coefficients are the same for all species.

2.2. Approximations of the thermodynamic properties and transport coefficients for the multispecies mixture

Thermodynamic relationships and transport coefficients are necessary to close the nonlinear system of governing equations. The fluid is assumed to be a thermally perfect, compressible gaseous mixture [21]. Thermodynamic and molecular transport properties of each gaseous species are prescribed using the empirical database compiled by Gordon et al. [22], and McBride and Gordon [23], which provides curve fits for the species enthalpy, specific heat, and entropy, as functions of temperature. The specific absolute enthalpy is evaluated by

$$h_n = \frac{H_n(T)}{M_n}. \quad (7)$$

The curve fit for the molar enthalpy of the n th species, $H_n(T)$, is given by

$$\frac{H_n(T)}{R_u T} = -\frac{a_{1,n}}{T^2} + \frac{a_{2,n}}{T} \ln T + a_{3,n} + \frac{a_{4,n} T}{2} + \frac{a_{5,n} T^2}{3} + \frac{a_{6,n} T^3}{4} + \frac{a_{7,n} T^4}{5} + \frac{a_{8,n}}{T}. \quad (8)$$

The coefficients are fit using data from the Joint-Army-Navy-Air Force (JANAF) Thermo-chemical Tables [24]. The viscosity (or thermal conductivity) for a particular species is given by

$$\ln \mu_n (\text{or } \kappa_n) = b_{1,n} \ln T + \frac{b_{2,n}}{T} + \frac{b_{3,n}}{T^2} + b_{4,n}. \quad (9)$$

In the above curve fits, $a_{1-8,n}$ and $b_{1-4,n}$ are the coefficients given for each species; note that values of $b_{k,n}$ are different for viscosity and conductivity. The mixture values of μ and κ are calculated using mixture-based formulas [25],

$$\mu = \frac{1}{2} \left[\sum_{n=1}^{N_s} \mu_n \chi_n + \left(\sum_{n=1}^{N_s} \frac{\chi_n}{\mu_n} \right)^{-1} \right],$$

and

$$\kappa = \frac{1}{2} \left[\sum_{n=1}^{N_s} \kappa_n \chi_n + \left(\sum_{n=1}^{N_s} \frac{\chi_n}{\kappa_n} \right)^{-1} \right],$$

where the mole fractions are defined by

$$\chi_n = \frac{c_n}{M_n \sum_{j=1}^{N_s} \frac{c_j}{M_j}}.$$

3. Fourth-order finite-volume method on mapped domains

3.1. The spatial and temporal discretization schemes

The focus of the present study is on the new schemes that facilitate the treatment of nonlinear thermodynamic and transport properties of the multispecies. More precisely, it concentrates on the development of new operators for the viscous flux evaluation. The semi-discrete form of the nonlinear system of governing PDEs is

$$\frac{d}{dt} (\mathbf{J}\mathbf{U})_i = -\frac{1}{h} \sum_{d=1}^D \left[\left(\langle \mathbf{N}_d^T \bar{\mathbf{F}} \rangle_{i+\frac{1}{2}\mathbf{e}^d} - \langle \mathbf{N}_d^T \bar{\mathbf{F}} \rangle_{i-\frac{1}{2}\mathbf{e}^d} \right) - \left(\langle \mathbf{N}_d^T \bar{\mathcal{G}} \rangle_{i+\frac{1}{2}\mathbf{e}^d} - \langle \mathbf{N}_d^T \bar{\mathcal{G}} \rangle_{i-\frac{1}{2}\mathbf{e}^d} \right) \right] + (\mathbf{J}\mathbf{S})_i. \quad (10)$$

Eq. (10) shows that the inviscid flux can be simply evaluated by multiplying the physical inviscid flux, $\bar{\mathbf{F}}$, with the grid metrics, \mathbf{N}^T . The semi-discrete form is used in the fourth-order Runge–Kutta time marching method [26] to advance the solution in time. Details of the inviscid flux evaluation on mapped grids can be found in our previous work [27]. It is worth noting that our recent work [28] investigated an average-based scheme for the viscous flux, $\bar{\mathcal{G}}$, evaluation. However, for multispecies mixing or reacting flows, where the thermodynamic and transport properties of gaseous mixtures are nonlinear and vary both temporally and spatially, an efficient and effective viscous flux evaluation is required.

The immediate goal is to determine the fourth-order accurate averages, $\langle \mathbf{N}_d^T \bar{\mathcal{G}} \rangle$, the mapped viscous flux in Eq. (10). This utilizes a product rule of the form (ϕ and ψ represent two arbitrary

variables)

$$\langle \phi \psi \rangle_{i+\frac{1}{2}\mathbf{e}^d} = \langle \phi \rangle_{i+\frac{1}{2}\mathbf{e}^d} \langle \psi \rangle_{i+\frac{1}{2}\mathbf{e}^d} + \frac{\Delta \xi_{d'}^2}{12} \sum_{d' \neq d} \frac{\partial \phi}{\partial \xi_{d'}} \frac{\partial \psi}{\partial \xi_{d'}} \Big|_{i+\frac{1}{2}\mathbf{e}^d} + O(\Delta \xi_d^4), \quad (11)$$

which is valid on general rectilinear grids [29]; therefore, Eq. (11) is valid on mapped rectilinear grids. To demonstrate an application of Eq. (11), we can evaluate the product of the face-averaged values, $\langle \mathbf{N}_d^T \bar{\mathcal{G}} \rangle_{i+\frac{1}{2}\mathbf{e}^d}$

$$\langle \mathbf{N}^T \bar{\mathcal{G}} \rangle_{i+\frac{1}{2}\mathbf{e}^d} = \langle \mathbf{N}^T \rangle_{i+\frac{1}{2}\mathbf{e}^d} \langle \bar{\mathcal{G}} \rangle_{i+\frac{1}{2}\mathbf{e}^d} + \frac{\Delta \xi_{d'}^2}{12} \sum_{d' \neq d} \frac{\partial \mathbf{N}^T}{\partial \xi_{d'}} \frac{\partial \bar{\mathcal{G}}}{\partial \xi_{d'}} \Big|_{i+\frac{1}{2}\mathbf{e}^d}, \quad (12)$$

where $\bar{\mathcal{G}}$ is a viscous flux vector of the flux dyad $\bar{\mathcal{G}}$ from one of the governing equations. For instance, in the ξ -momentum equation, $\bar{\mathcal{G}}$ in three dimensions takes the form of

$$\begin{aligned} \bar{\mathcal{G}} = & \mu \left(2 \frac{\partial u_0}{\partial \xi_d} \frac{\mathbf{N}_{d0}^T}{J} - \frac{1}{3} \frac{1}{J} \frac{\partial (\mathbf{N}_{dd}^T u_d)}{\partial \xi_d} \right) \bar{\xi} \\ & + \mu \left(\frac{\partial u_0}{\partial \xi_d} \frac{\mathbf{N}_{d1}^T}{J} + \frac{\partial u_1}{\partial \xi_d} \frac{\mathbf{N}_{d0}^T}{J} \right) \bar{\eta} \\ & + \mu \left(\frac{\partial u_0}{\partial \xi_d} \frac{\mathbf{N}_{d2}^T}{J} + \frac{\partial u_2}{\partial \xi_d} \frac{\mathbf{N}_{d0}^T}{J} \right) \bar{\zeta}. \end{aligned} \quad (13)$$

Note that the integer indices 0, 1, and 2, correspond to ξ , η , and ζ , respectively.

The mapped viscous flux, $\langle \mathbf{N}_d^T \bar{\mathcal{G}} \rangle$, can be readily computed using Eq. (12), given the information of $\langle \mathbf{N}_d^T \rangle$, $\langle \bar{\mathcal{G}} \rangle$, $\frac{\partial \mathbf{N}^T}{\partial \xi_{d'}}$, and $\frac{\partial \bar{\mathcal{G}}}{\partial \xi_{d'}}$. Therefore, the task is now to calculate fourth-order estimates of $\langle \mathbf{N}_d^T \rangle$ and $\langle \bar{\mathcal{G}} \rangle$, and second-order estimates of $\frac{\partial \mathbf{N}^T}{\partial \xi_{d'}}$ and $\frac{\partial \bar{\mathcal{G}}}{\partial \xi_{d'}}$. The face-averaged values of $\langle \mathbf{N}_d^T \rangle$ and $\langle \bar{\mathcal{G}} \rangle$ can be converted from the face-centered values using a fourth-order approximation

$$\langle \bar{\mathcal{G}} \rangle_{i+\frac{1}{2}\mathbf{e}^d} = \bar{\mathcal{G}}_{i+\frac{1}{2}\mathbf{e}^d} + \frac{\Delta \xi_{d'}^2}{24} \sum_{d' \neq d} \frac{\partial^2 \bar{\mathcal{G}}}{\partial \xi_{d'}^2} \Big|_{i+\frac{1}{2}\mathbf{e}^d}. \quad (14)$$

Clearly, computing the face-centered viscous flux and its second derivative in the direction orthogonal to the face is the aim.

3.2. The interior spatial discretization scheme

The interior scheme includes the following sequential operations to compute the face-centered viscous flux and its second, transverse derivative. The procedure is demonstrated here using velocity but is applicable for any primitive variable.

1. Find the face-centered velocity gradients from the face-averaged velocity gradients using

$$\left(\frac{\partial \bar{u}}{\partial \xi_{d'}} \right)_{i+\frac{1}{2}\mathbf{e}^d} = \left\langle \frac{\partial \bar{u}}{\partial \xi_{d'}} \right\rangle_{i+\frac{1}{2}\mathbf{e}^d} - \frac{\Delta \xi_{d'}^2}{24} \Delta^{\perp,d} \left\langle \frac{\partial \bar{u}}{\partial \xi_{d'}} \right\rangle_{i+\frac{1}{2}\mathbf{e}^d}, \quad (15)$$

where the transverse Laplacian (demonstrated with a quantity ϕ) is given by

$$\Delta^{\perp,d} \phi_{i+\frac{1}{2}\mathbf{e}^d} = \sum_{d' \neq d} \frac{1}{\Delta \xi_{d'}^2} \left(\phi_{i+\frac{1}{2}\mathbf{e}^d - \mathbf{e}^{d'}} - 2\phi_{i+\frac{1}{2}\mathbf{e}^d} + \phi_{i+\frac{1}{2}\mathbf{e}^d + \mathbf{e}^{d'}} \right). \quad (16)$$

Fig. 1 depicts the stencil to compute the fourth-order accurate, face-centered, tangential gradient of velocity from cell-averaged velocity values using Eqs. (15) and (16). Specifically, the figure shows the information radius required to evaluate the face-centered tangential gradients of velocity on the $i+\frac{1}{2}\mathbf{e}^d$ face. This methodology also holds for finding the face-centered, normal gradients of velocity.

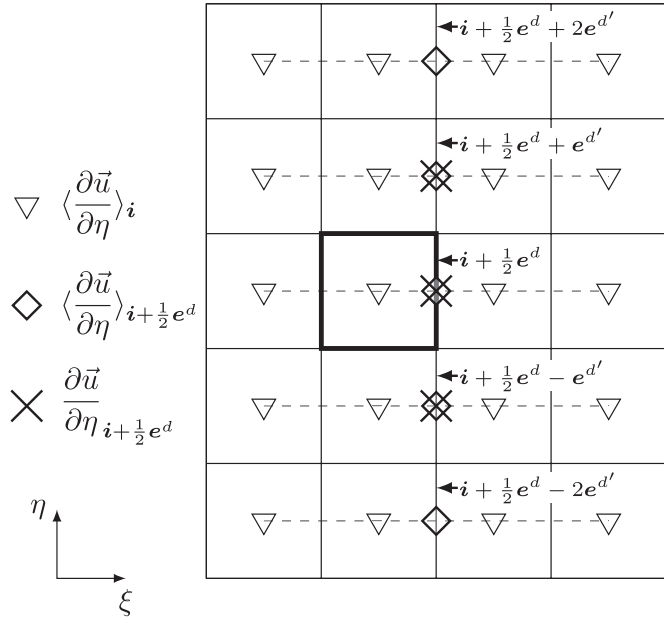


Fig. 1. The stencil for computing the face-centered $\frac{\partial \vec{u}}{\partial \eta}$ on a ξ -face of the cell highlighted by bold black lines.

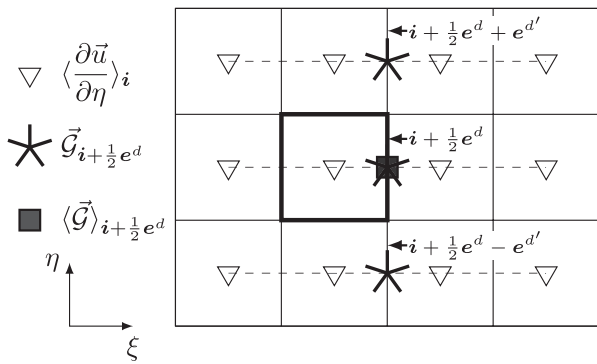


Fig. 2. The stencil for computing the face-centered elliptic flux on a ξ -face of the cell marked by bold black lines.

2. Compute $\vec{G}_{i+\frac{1}{2}e^d}$, the viscous flux vector. Refer to Eq. (13). The metrics Jacobian and grid metrics are the face-centered values, which are readily provided from the physical geometric information.
3. Evaluate a second-order tangential derivative of $\vec{G}_{i+\frac{1}{2}e^d}$, using the center differencing equation,

$$\left(\frac{\partial \vec{G}}{\partial \xi_{d'}} \right)_{i+\frac{1}{2}e^d} = \frac{1}{2\Delta \xi_{d'}} \left(\vec{G}_{i+\frac{1}{2}e^d+e^{d'}} - \vec{G}_{i+\frac{1}{2}e^d-e^{d'}} \right). \quad (17)$$

This will be used in Eq. (12).

4. Calculate $\langle \vec{G} \rangle_{i+\frac{1}{2}e^d}$ from $\vec{G}_{i+\frac{1}{2}e^d}$ using Eq. (14). Fig. 2 illustrates the stencil to calculate $\langle \vec{G} \rangle_{i+\frac{1}{2}e^d}$.
5. Obtain $\langle N^T \vec{G} \rangle$ using the result from Eq. (17) in Eq. (12), then readily compute $\langle N^T \vec{G} \rangle$.

Note that $\langle N^T \rangle$ and $\frac{\partial N^T}{\partial \xi_{d'}}$ are treated in the same manner. The above is described for interior stencils. Methodology for handling physical boundaries is detailed in Gao et al. [28] and Owen et al. [30] and will not be repeated here.

3.3. Comments on several aspects of the present algorithm

Our numerical framework makes use of Chombo [31], a highly parallel AMR library. The parallel performance and scalability of the base framework are evaluated and reported in our previous work by Guzik et al. [32]. Other important aspects of the algorithm, including mapped grids, solid physical boundaries, and freestream preservation, are detailed in our previous studies [27,28,32].

The AMR method is block-structured and subcycling is employed. Subcycling occurs in the refined regions, meaning the finer level takes a number of time steps equal to the refinement ratio between the levels for every time step on the coarse level. More information regarding the AMR and subcycling methodology is provided by Berger and Colella [33] and Guzik et al. [27].

3.4. Warped mapping

In order to validate the mapping functionality, test cases are run with artificial mapping. The mapping is based on the length of the domain, \bar{L} , and a scaling factor, \bar{S} , to allow the mapping to apply to a wider range of problems. The computational grid is artificially warped according to the mapping

$$x_d = \xi_d + S_d \prod_{p=1}^D \sin \left(\frac{2\pi \xi_p}{L_p} \right), \quad d = 1, \dots, D. \quad (18)$$

The order of accuracy of mapped solutions is preserved so long as the mapping functionality remains continuous and smooth on the grid resolution within the domain. To ensure the warped mesh does not tangle, it is sufficient to take $\forall d, 0 \leq 2\pi S_d \leq L_d$. More information regarding this specific mapping is provided by Colella et al. [34].

3.5. Refinement criteria

Areas of interest, such as combustion flame fronts, should use a finer mesh in order to reduce the error. AMR allows us to refine around areas of interest without increasing the computational costs associated with using a mesh of the finest resolution throughout the entire domain. For the cases described in this paper, the mesh is refined based on a normalized gradient of a variable (e.g. density), arbitrarily denoted as ϕ , using

$$\delta \phi_i = \sqrt{\sum_{d=1}^D \left(\frac{\phi_{i+e^d} - \phi_{i-e^d}}{\phi_{i+e^d} + \phi_{i-e^d}} \right)^2}, \quad (19)$$

and a refinement threshold, δ_r . If $\delta \phi_i > \delta_r$, then that particular cell is tagged for refinement. If multiple refinement criteria are specified, regions are tagged for refinement if any of the criteria are satisfied.

Although the refinement criteria detailed above is sufficient for the current work, we suspect more sophisticated refinement criteria would further reduce the computational expense. It is important that the new refinement criteria are consistent with the fourth-order accuracy of the underlying numerical algorithm. Currently, we are exploring refinement tagging based on the gradient field of the vorticity magnitude as well as the second derivatives of scalar fields. The results will be reported in a future study.

4. Verification & validation

To verify and validate the algorithm for solving thermally-perfect, multispecies flows on mapped domains, five problems are solved: shock tube, shock box, Couette flow, species mass diffusion bubble, and vortex convection and diffusion problem. Freestream preservation is verified using a uniform flow in a domain with periodic boundaries.

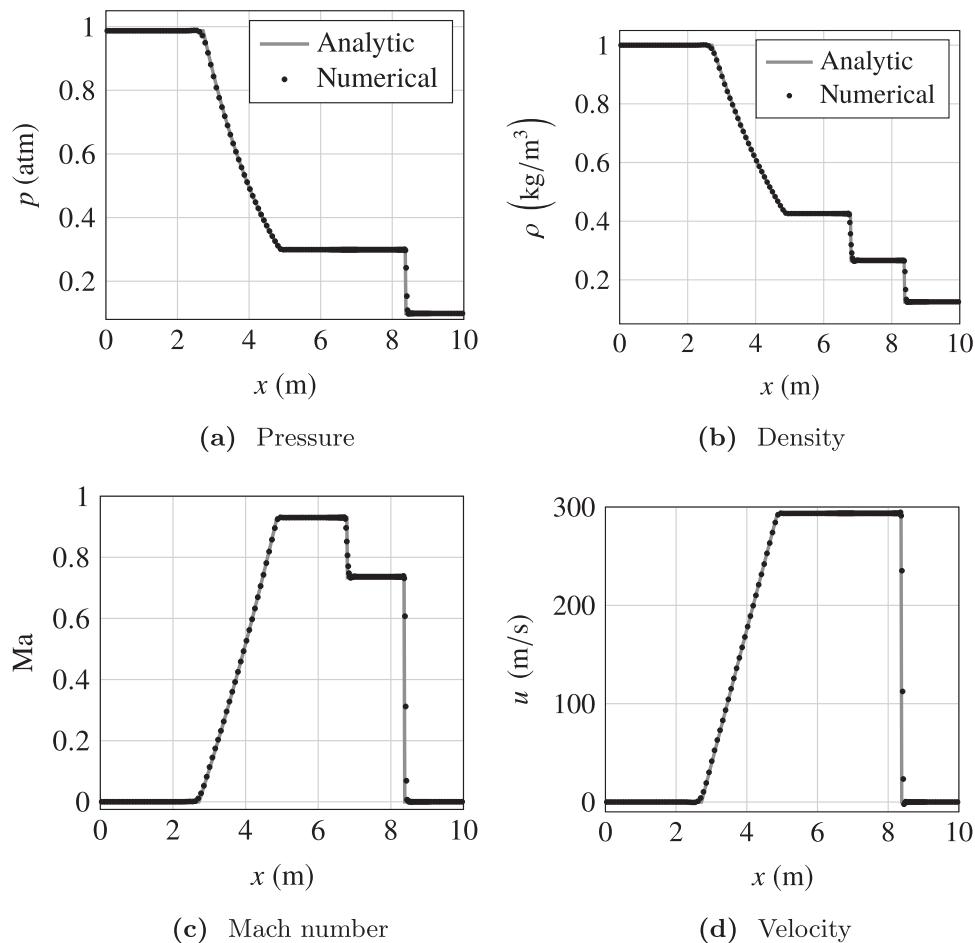


Fig. 3. Solution to the shock tube problem at $t = 6.1$ ms.

4.1. Multispecies shock tube problem

The one-dimensional shock tube problem is a classic case used to validate convective fluxes with strong discontinuities as it has an analytical solution. The problem consists of a left and right region of stagnant gas. One region is initialized at a high pressure and density relative to the other region. This initialization produces a shock that travels into the low pressure and density region.

The right portion of the domain is initialized as a low region of $\rho_R = 0.125$ kg/m³ and $p_R = 1 \times 10^4$ Pa and the left portion is initialized as a high region of $\rho_L = 8\rho_R$ and $p_L = 10p_R$. The fluid in the domain is a uniform mixture of $c_{O_2} = 0.233$ and $c_{N_2} = 0.767$.

The domain is $10 \text{ m} \times 0.625 \text{ m}$ with a base computational grid of 128×8 cells. Two additionally refined levels with refinement ratios of 2 for each level are applied. The grid is dynamically refined using Eq. (19) based on gradients of density with $\delta_t = 0.05$. Subcycling is used during the solution. The boundaries are periodic in the y -direction and extrapolated in the x -direction.

The test is run to time $t = 6.1$ ms and compared with the analytical solution. Fig. 3 shows good agreement between the analytical and numerical solutions with no severe oscillations occurring at the discontinuities, thus validating the algorithm accurately captures shock physics.

4.2. Multispecies shock box problem

The shock box extends the shock tube problem to two dimension, allowing for multi-dimensional shocks convecting and interacting within the domain.

The $1 \text{ m} \times 1 \text{ m}$ domain is initialized with fluid mixture of $c_{O_2} = 0.233$ and $c_{N_2} = 0.767$, and the fluid is quiescent at the initial state. The lower left quarter of the domain is initialized to $\rho_L = 1.225$ kg/m³ and $p_L = 1$ atm and the rest of the domain is initialized to $\rho_U = 4\rho_L$ and $p_U = 4p_L$. The subscripts U and L represent the upper and the lower regions, respectively.

The computational mesh uses a base grid of 128×128 with two additionally refined levels with refinement ratios of 2 for each level. The grid is dynamically refined using Eq. (19) based on gradients of density and pressure with $\delta_t = 0.1$. Again, subcycling is used during the solution. The boundaries are all slip walls. To test the mapping functionality, the grid is artificially warped according to Eq. (18), where $S_d = 0.075$.

The case is run to time $t = 2$ ms. At this solution time, the shocks in the x and y -directions have converged in the lower left corner and reflected back into the domain. Fig. 4 shows the solution pressure in units of atm with an overlay of the mesh. Fig. 4(a) and (b) show the solutions in physical and computational spaces, respectively. The mesh in Fig. 4(a) demonstrates the warping imposed by Eq. (18). Similarly, Fig. 5 shows the solution of the Mach number in physical and computational space. The solutions agree well with literature results [35].

4.3. Multispecies Couette flow problem

Couette flow is used to verify the order of accuracy of the molecular viscous operators. Couette flow is defined as flow between two parallel no-slip walls; one wall is stationary and the other wall is moving at a set velocity. The fluid is a mixture

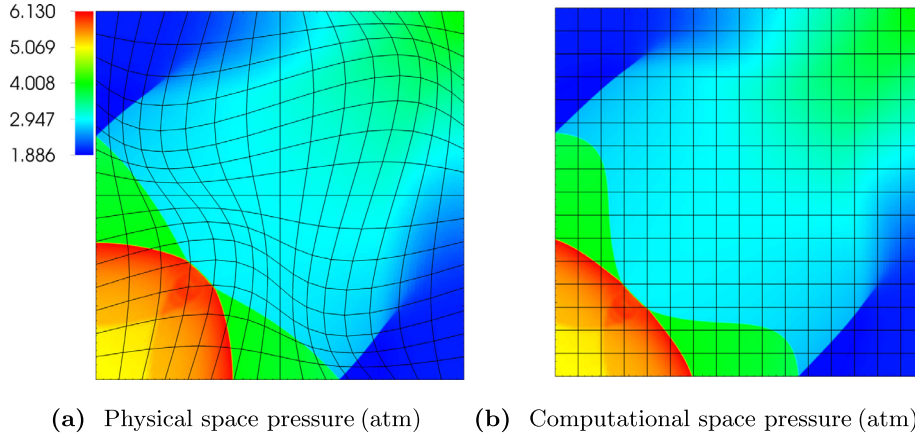


Fig. 4. Solution of pressure in physical and computational space with demonstration of mesh overlay at solution time $t = 2$ ms.

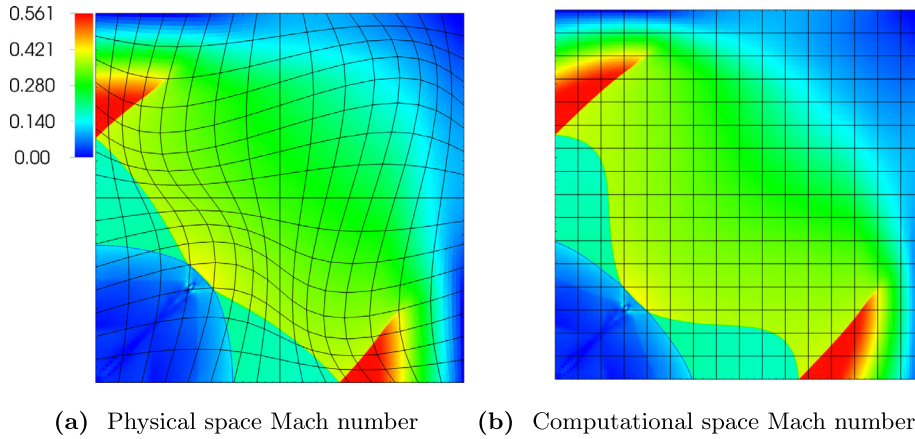


Fig. 5. Solution Mach number in physical and computational space with demonstration of mesh overlay at solution time $t = 2$ ms.

of $c_{O_2} = 0.233$ and $c_{N_2} = 0.767$. The domain length is $L_x \times L_y = 5.456 \text{ mm} \times 5.456 \text{ mm}$ and is periodic in the x -direction. The velocity of the wall in the lower y -direction is calculated using

$$U_{\text{wall}} = \frac{\text{Re}\mu}{\rho L_y},$$

where $\mu = 1.7894 \times 10^{-5} \text{ kg/(m}\cdot\text{s)}$, $\rho = 1.0 \text{ kg/m}^3$, and $\text{Re} = 1000$.

Again, the grid is artificially warped according to Eq. (18), where $S_d = 0.075$. Since Couette flow has a known analytical solution, we compare the norms of the error between the numerical solution and analytical solution on four grids of sizes 64×64 , 128×128 , 256×256 , and 512×512 . The initial condition is the analytical solution at time $t = 0.2$ ms and solved to a time of $t = 0.202496$ ms.

Errors are measured with the L_∞ -, L_1 -, and L_2 -norms of the difference between the analytical solution and the numerical solution. The norms are computed using,

$$L_m = \begin{cases} \max(|\phi_i^{\text{exact}} - \phi_i|) & \text{if } m = \infty \\ \left(\sum_i |\phi_i^{\text{exact}} - \phi_i|^m \right)^{(1/m)} \left(\prod_{d=1}^D N_d \right)^{(-1/m)} & \text{otherwise} \end{cases}, \quad (20)$$

where ϕ_i is the numerical solution of any conservative variable (such as ρ , ρu , or ρe), ϕ_i^{exact} is the exact (or analytical) solution of the conservative variable, and N_d is the number of cells in the d th direction.

The solution error norms and convergence rates are shown in Table 1. As expected, the norms of the solution errors decrease as the grid is refined. The convergence rates for all norms and solutions are above 4, demonstrating fourth-order accuracy of the discrete operators for the momentum diffusion for the thermally-perfect, multispecies algorithm on a warped grid.

4.4. Multispecies mass diffusion bubble problem

To verify the mass diffusion operations, we solve a two-dimensional species mass diffusion problem on a $1 \text{ m} \times 1 \text{ m}$ periodic domain. A circle of radius r_c that is centered at location (x_c, y_c) is initialized to values designated as region 2 and the remainder of the domain is initialized to values designated to region 1. The initial conditions are demonstrated in Fig. 6 where regions 1 and 2 are labeled and shaded region represents the smooth interface between the regions. The domain is initialized to a uniform pressure of 101,325 Pa. The initialization values are: $T_1 = 298 \text{ K}$, $T_2 = 310 \text{ K}$, $(c_{O_2})_1 = (c_{N_2})_2 = 0.233$, $(c_{O_2})_2 = (c_{N_2})_1 = 0.767$, and $r_c = 0.1 \text{ m}$. The initial density is given by the ideal gas law.

The domain is initialized to a uniform pressure. The values of T , c_{O_2} , and c_{N_2} are initialized using a smoothing function, defined by

$$\phi = \phi_1 + \frac{1}{2}(1 + \tanh[(r_c - r)100])(\phi_2 - \phi_1),$$

where ϕ is the initial value of the variables for T and c_n , ϕ_1 is initial value for region 1, ϕ_2 is the initial value in region 2, and r

Table 1

Numerical values of the Couette flow solution errors measured with the L_∞ -, L_1 -, and L_2 -norms at 0.202496 ms and the convergence rates between consecutive grid resolutions.

Var	$L_\#$ -norm	64×64	Rate	128×128	Rate	256×256	Rate	512×512
ρu	L_∞	3.471e-04	4.663	1.370e-05	5.020	4.222e-07	5.043	1.280e-08
	L_1	8.574e-13	4.964	2.748e-14	4.538	1.183e-15	4.206	6.405e-17
	L_2	1.159e-08	5.168	3.225e-10	5.254	8.454e-12	4.757	3.127e-13
ρv	L_∞	2.595e-05	4.788	9.397e-07	5.158	2.631e-08	4.714	1.003e-09
	L_1	1.428e-13	4.441	6.572e-15	4.200	3.575e-16	4.081	2.113e-17
	L_2	1.065e-09	4.869	3.645e-11	4.554	1.551e-12	4.186	8.523e-14

Table 2

Numerical values of the mass diffusion solution errors measured with the L_∞ -, L_1 -, and L_2 -norms at 4.4928 s and the convergence rates between consecutive grid resolutions.

Var	$L_\#$ -norm	64×64	Rate	128×128	Rate	256×256	Rate	512×512
ρe	L_∞	1.271e+02	3.100	1.482e+01	3.684	1.153e+00	3.992	7.249e-02
	L_1	1.951e+00	3.725	1.476e-01	3.823	1.043e-02	3.948	6.756e-04
	L_2	1.112e+01	3.556	9.449e-01	3.790	6.832e-02	3.947	4.430e-03
ρc_{O_2}	L_∞	3.067e-03	4.206	1.661e-04	3.750	1.234e-05	3.939	8.046e-07
	L_1	5.850e-05	3.889	3.948e-06	3.876	2.688e-07	3.970	1.716e-08
	L_2	2.959e-04	3.988	1.865e-05	3.858	1.286e-06	3.963	8.249e-08
ρc_{N_2}	L_∞	2.656e-03	3.947	1.722e-04	3.810	1.227e-05	3.942	7.987e-07
	L_1	5.506e-05	3.909	3.664e-06	3.885	2.481e-07	3.968	1.585e-08
	L_2	2.668e-04	3.956	1.719e-05	3.856	1.187e-06	3.960	7.628e-08

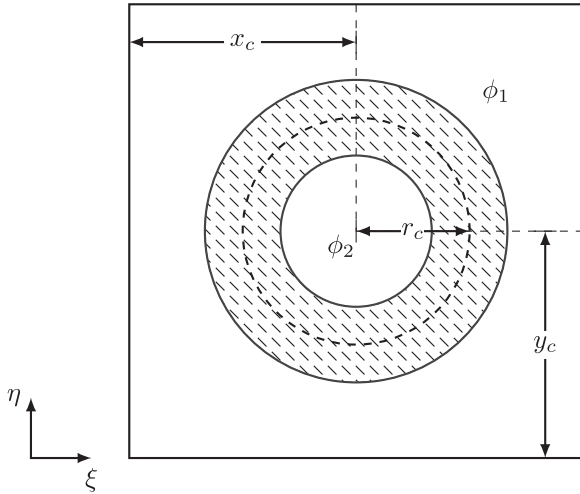


Fig. 6. Demonstration of the initialization of the two regions for the diffusion bubble problem. The shaded region represents the smooth interface between regions 1 and 2.

is the radius. The radius is given by

$$(\bar{x}, \bar{y}) = (x - x_c, y - y_c), \quad r = \sqrt{\bar{x}^2 + \bar{y}^2}. \quad (21)$$

The center of the bubble is at $(x_c, y_c) = (0.5, 0.5)$. The mass diffusion is solved using Eq. (6) with a constant Lewis number of $Le = 0.7$.

Numerical solution errors are measured with the L_∞ -, L_1 -, and L_2 -norms at $t = 4.4928$ s. The convergence rates between consecutive grid resolutions are computed using Richardson extrapolation, as described in Guzik et al. [27]. The pre-coarse, coarse, medium, and fine meshes are 64×64 , 128×128 , 256×256 , and 512×512 , respectively. The post-fine solution on a 1024×1024 mesh is used as a “true” solution for computing the error norms during the Richardson extrapolation procedure, meaning the post-fine values represent the values of ϕ_i^{exact} in Eq. (20). The time step for the coarse grid is 0.0432 s and is adjusted proportionally depending on the change in grid size. Table 2 lists the error norms and the corresponding rates in the error reduction as the grid is refined for conservative solution variables (density, momentum, en-

ergy) from then on. As expected, the norms of the solution error decrease as the grid is refined. Clearly, the error reduction rates for the solution variables are all converging toward 4, indicating the discretization operators for the species mass diffusion and the thermal diffusion are fourth-order accurate.

4.5. Vortex convection and diffusion problem

The numerical solution accuracy is verified using a two-dimensional vortex convection and diffusion problem, similar to the one described by Yee et al. [36]. The vortex problem is selected for evaluating the algorithm accuracy and performance due to the absence of shock waves and turbulence. The fluid is a uniform mixture of oxygen and hydrogen, $c_{O_2} = 0.233$ and $c_{H_2} = 0.767$.

The vortex center, (x_c, y_c) , vortex strength, Γ , stagnation temperature, T_∞ , and stagnation pressure, p_∞ , are all specified. For the uniform initial mixture mass fractions, the gas constant is $R_\infty = \sum c_n R_n$. The radius is given by Eq. (21). The initial velocity is perturbed using

$$(u, v) = (u_\infty - \bar{y}v_\theta, v_\infty + \bar{x}v_\theta),$$

where

$$v_\theta = \frac{\Gamma}{2\pi} \exp\left(\frac{1-r^2}{2}\right).$$

The pressure is initialized using

$$p = p_\infty \left(1 - \left(\frac{\Gamma}{2\pi}\right)^2 \left(\frac{\exp(1-r^2)}{2T_\infty R_\infty}\right)\right). \quad (22)$$

The initial temperature is solved using the isentropic relation

$$T = T_\infty \left(\frac{p}{p_\infty}\right)^{\frac{\gamma-1}{\gamma}}, \quad (23)$$

assuming a constant γ . The density is initialized using the ideal gas law

$$\rho = \frac{p}{TR_\infty}.$$

Accuracy verification is performed on a vortex case where $T_\infty = 2900$ K, $p_\infty = 101,325$ Pa, and $\Gamma = 20$ m²/s. The values are chosen in an effort to minimize the Reynolds number while maintaining

Table 3

Numerical values of the stationary vortex solution errors measured with the L_∞ -, L_1 -, and L_2 -norms at 0.08449 s and the convergence rates between consecutive grid resolutions.

Var	L norm	128×128	Rate	256×256	Rate	512×512	Rate	1024×1024
ρ	L_∞	1.791e-10	2.897	2.405e-11	4.137	1.367e-12	3.987	8.616e-14
	L_1	4.061e-11	2.748	6.047e-12	3.958	3.891e-13	3.988	2.453e-14
	L_2	5.350e-11	2.782	7.780e-12	3.976	4.944e-13	3.989	3.114e-14
ρu	L_∞	3.952e-05	5.028	1.212e-06	3.965	7.758e-08	3.994	4.871e-09
	L_1	3.793e-07	3.935	2.480e-08	3.996	1.555e-09	3.989	9.789e-11
	L_2	1.769e-06	4.662	6.987e-08	3.979	4.432e-09	3.994	2.781e-10
ρe	L_∞	6.507e-03	2.897	8.735e-04	4.137	4.963e-05	3.987	3.130e-06
	L_1	1.475e-03	2.747	2.196e-04	3.958	1.413e-05	3.988	8.911e-07
	L_2	1.943e-03	2.782	2.826e-04	3.976	1.796e-05	3.989	1.131e-06

a perturbation in pressure, density, and temperature. The Reynolds number is minimized to ensure the flow is laminar and to increase the diffusive fluxes influence on the solution. The vortex is stationary, meaning $u_\infty = v_\infty = 0$ m/s. The transport properties values are computed by Eq. (9) and are initially at $\mu = 4.515 \times 10^{-5}$ kg/(m·s) and $\kappa = 1.084$ W/(m·K). The non-dimensional values are given by

$$\text{Re} = \frac{\rho \Gamma}{\mu}, \quad \text{Ma} = \frac{|u|_{\max}}{a} = \frac{\Gamma/(2\pi)}{\sqrt{\gamma RT_\infty}}, \quad \text{and} \quad \text{Pr} = \frac{\mu c_p}{\kappa}.$$

The values for this particular case are $\text{Re} = 4800$, $\text{Ma} = 9.16 \times 10^{-4}$, and $\text{Pr} = 0.596$.

The computational domain is a $30 \text{ m} \times 30 \text{ m}$ square and periodic boundary conditions are enforced at both of the domain extents. The vortex center is located at the middle of the domain, $(x_c, y_c) = (15, 15)$. Numerical solution errors are measured with the L_∞ -, L_1 -, and L_2 -norms at $t = 0.084488$ s. The convergence rates between consecutive grid resolutions are computed using Richardson extrapolation, as described in Guzik et al. [27]. The pre-coarse, coarse, medium, and fine meshes are 128×128 , 256×256 , 512×512 , and 1024×1024 , respectively. The post-fine solution on a 2048×2048 mesh is used as a “true” solution for computing the error norms during the Richardson extrapolation procedure. The time step for the coarse grid is 2.1122×10^{-5} s and is adjusted proportionally as the grids are refined (1.0561×10^{-5} s for the medium grid etc.). The solution is run to solution time $t = 0.084488$ s. Table 3 lists the error norms and the corresponding rates in the error reduction as the grid is refined for conservative solution variables (density, momentum, energy) from then on. Convergence rates of 4 for all solution variables verify the algorithm is fourth-order accurate.

4.6. Freestream preservation

The freestream preservation test is conducted on a doubly periodic domain initialized with a uniform velocity, density, pressure, and species mass fractions. In order to fully test freestream preservation, a warped mapping with two levels of moving AMR are used as shown in Fig. 7. This takes place on a base grid of 64×64 cells over 1000 time steps, corresponding to 1×10^{-3} s. Over this period of time, the refinement region makes one circular rotation in the computational space about the center of the domain.

For each of the conservative variables, the initial state and the final state at the chosen run time are compared using an L_1 -norm. The difference between the values is computed in order to quantify error present in the solution, as, ideally, the freestream case will have no change in states. Table 4 clearly demonstrates that the freestream condition is preserved. Moreover, we computed the difference between the L_1 -norms from over the solution time and the norms are all close to machine zero. This verifies that the freestream preservation is maintained.

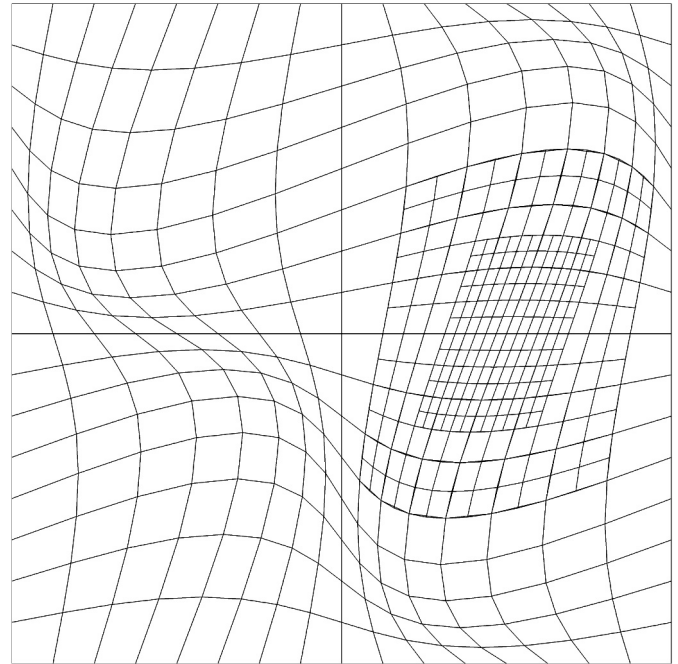


Fig. 7. Demonstration of the mapped grid in physical space with refinement regions for the freestream preservation test.

5. Numerical simulation results and discussions

The verified algorithm is now applied to simulate two multi-species flow problems: the Mach reflection shock ramp and the jet mixing flow. There are three purposes for solving these problems. First, the presence of strong shock waves in the flow necessitates the use of a limiter in the hyperbolic flux evaluation process to suppress oscillations. Second, the algorithm is demonstrated on a non-rectangular physical domain. Lastly, the configurations represent more realistic boundary conditions, allowing a secondary mixing flow to be investigated. The Mach reflection and the jet mixing cases are run on nodes featuring two Intel E5-2670 v2 CPUs and 128GB of DRAM memory. Each node has 20 processing cores.

5.1. Multispecies Mach reflection problem

A Mach reflection problem is considered in order to demonstrate the capability of the algorithm to solve a thermally-perfect multispecies flow on a non-rectangular physical domain. The present solution is compared to the experimental data published by Ben-Dor and Glass [37]. For this particular case, we do not expect the current solution to differ from the single species, calorically perfect solution by Gao et al. [28].

Table 4

Comparison of the volume-averaged L_1 -norm of initial and final states of a multispecies freestream case, and the calculated solution difference.

Var	Initial	Final	Difference
ρ	1.22500000000000120e+0	1.22500000000000098e+0	0.00000000000000022e+0
ρu	2.45000000000000079e-1	2.44999999999982288e-1	0.00000000000017791e-1
ρv	2.45000000000000079e-1	2.44999999999979318e-1	0.00000000000020761e-1
ρe	1.10183777676502243e+5	1.10183777676502243e+5	0.00000000000000000e+5
ρc_{O_2}	6.12500000000000600e-1	6.12500000000000488e-1	0.00000000000000111e-1
ρc_{N_2}	6.12500000000000600e-1	6.12500000000000488e-1	0.00000000000000111e-1

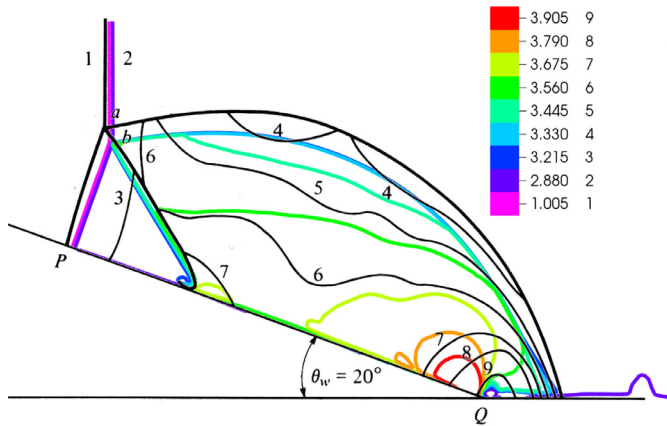


Fig. 8. Computed relative density (ρ/ρ_0) contours are shown in color. Experimental results are shown in black contours and are reproduced from Ben-Dor and Glass [37] (used with permission).

The ramp geometry, the physical and the computational domain, and the initial conditions in the present study, including the shock Mach number and the flow conditions in front of and behind the shock, are the same as those in Gao et al. [28], except the gas in the present study is comprised of $c_{Ar} = 0.99$ and $c_{N_2} = 0.01$ to validate the implementation of the multispecies functionality.

The computational grid has a 96×24 base grid with 2 levels of AMR, each refined by a factor of 4. Cells are tagged for refinement based on a gradient of density. All cells near the wall boundary are also tagged for refinement to ensure resolution of the boundary layer. The case is run on a single node with 20 processing cores for a wall-clock time of 11 min.

Fig. 8 quantitatively compares the numerical solution density contours against the experimental results published by Ben-Dor and Glass [37] at a time of 0.107 ms. Note, the density contours in Fig. 8 are relative to the freestream density, $\rho_1 = \rho_0 = 0.04354 \text{ kg/m}^3$. The present simulation agrees with our previous study [28] and shows general agreement with the experiment. Due to the similarities between the calorically perfect and thermally perfect numerical solutions, a detailed analysis of the simulation can be found in Gao et al. [28] and will not be repeated here.

5.2. Multispecies jets mixing problem

Flow mixing inside a two-dimensional burner geometry [38] is considered to demonstrate the capability of the algorithm to solve a thermally-perfect multispecies flow in a configuration with more realistic boundary conditions. Fig. 9 shows the two-dimensional burner geometry and the computational domain. A fuel-air mixture flows in the positive y -direction between two vertical walls, while air is injected horizontally from two jets located on the vertical walls. The height and width of the burner geometry are denoted by L_y and L_x , respectively, and are 0.1016 m. The distance from the bottom of the burner to the bottom of the jet, denoted by L_w , is

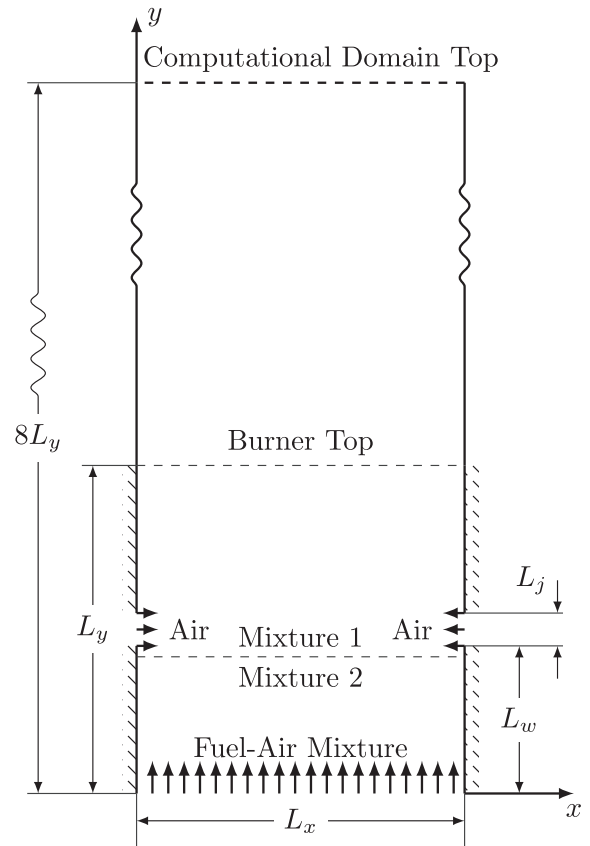


Fig. 9. The burner and computational domain geometry.

0.0492 m. The height of the jets, denoted by L_j , is 1.6×10^{-3} m. The computational domain has dimensions of $L_x \times 8L_y$. The computational domain extends beyond the top of the burner geometry in the y -direction to set the outlet boundary far from the top of the burner geometry, ensuring minimum interference on the outflow from the interior flow.

The fuel-air mixture consists of 5.51% CH_4 , 22.02% O_2 , and 74.47% N_2 by mass fraction and flows into the domain from the lower y boundary with a y -velocity of 0.075 m/s at a temperature of 313 K. At this boundary, the pressure is extrapolated from the interior of the domain. Air, consisting of 23.30% O_2 and 76.70% N_2 by mass fraction, is horizontally injected into the domain from the jets with a velocity of 4.96 m/s at a temperature of 293 K. At this boundary, pressure is again extrapolated from the interior. The walls are no-slip for $y < L_y$ but slip for $y \geq L_y$. The outlet uses a zero gradient Neumann condition for all variables. The initial mixture in the domain is quiescent. In the interior area where $y \geq 0.04\text{m}$, labeled “Mixture1” in Fig. 9, the initial fluid consists of 15.14% CO_2 , 12.39% H_2O and 72.46% N_2 at a temperature of 298 K. The remainder of the initial fluid in the domain, labeled “Mixture2” in Fig. 9,

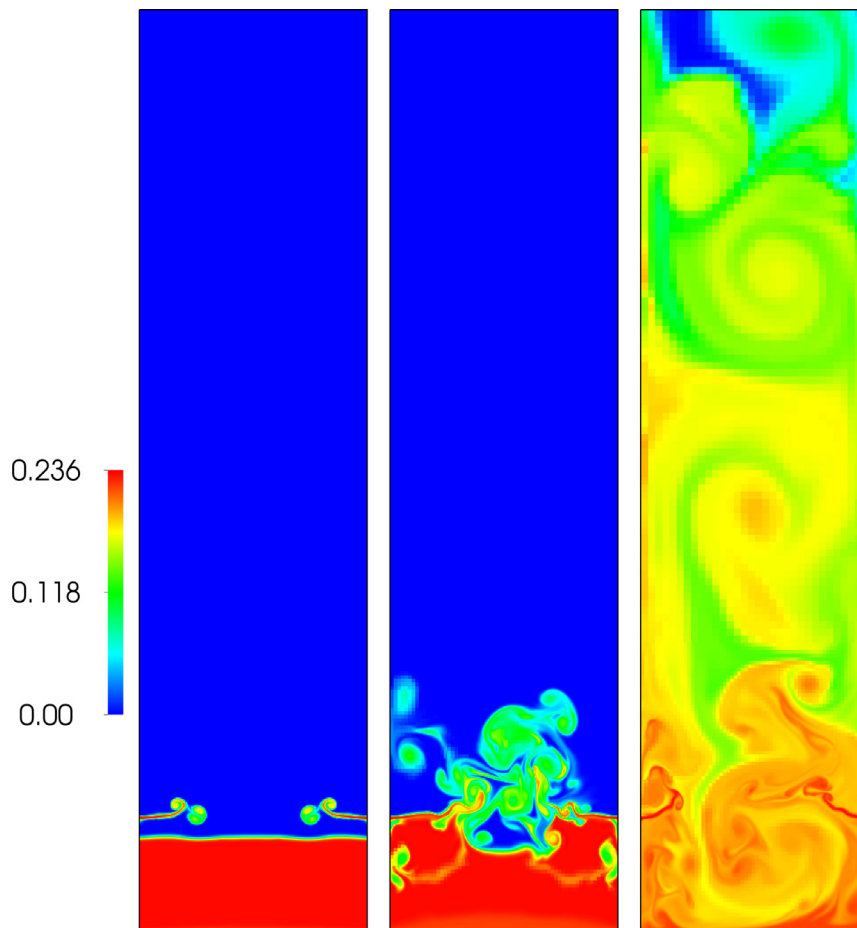


Fig. 10. Contour of mass fraction of O_2 of the lower half of the computational domain at $t = 0.02$ s, 0.101 s, and 1.652 s, respectively.

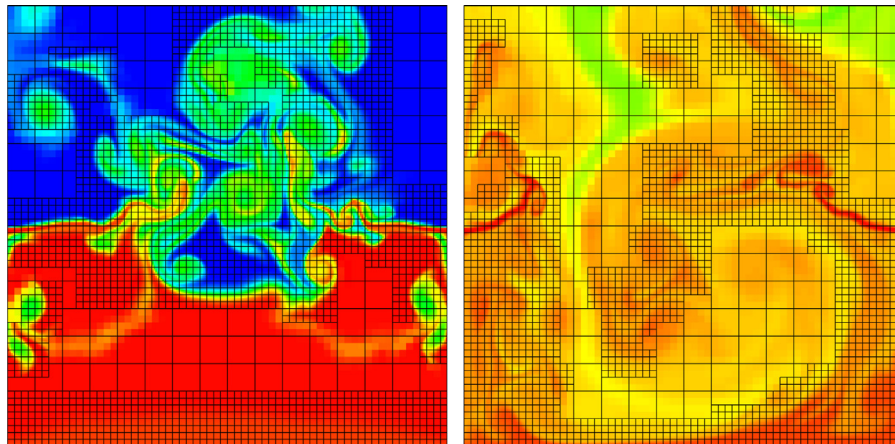


Fig. 11. Demonstration of the grid adaption at $t = 0.02$ s and 1.652 s, respectively. The mesh in the figure has been coarsened for display purposes.

is set to the same composition and temperature as the air from the jets. Both “Mixture1” and “Mixture2” are set to atmospheric pressure. The Reynolds number is 610 based on the jet inlet stream condition and 493 based on the syngas inflow condition.

The base grid is 32×256 with 2 additional refinement levels. The first level is refined 2 times and the second level is refined 4 times. Cells are dynamically tagged for refinement based on a gradient of density. The time step, dynamic viscosity, thermal conductivity, and diffusion coefficient are calculated using the methods outlined in Section 2. Subcycling is used during the solution. The solution is run for one convective time scale, i.e. the time re-

quired for the inflow to reach the top of the burner, which is approximately 1.345 s. The case is run on two nodes, totaling 40 processors, for a wall-clock time of 312 h.

Fig. 10 illustrates the distribution and evolution over time of the O_2 mass fractions for the lower half of the computational domain. The mesh adaption is demonstrated in Fig. 11 for two times, $t = 0.02$ s and 1.652 s. The mesh is adapted based on the physics criteria such as vorticity and species gradients. Note that in the figure, the meshes are only shown for the coarse levels for the purpose of a clear display. Fig. 12 is a close-up view of the burner geometry and shows the fluid structures produced by the jets and the fluid

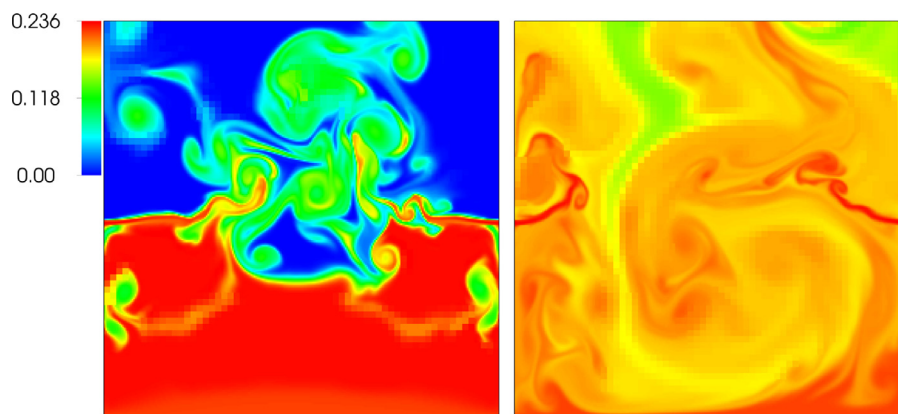


Fig. 12. Contour of mass fraction of O_2 of the burner geometry at $t = 0.101$ s and 1.652 s, respectively.

interactions between the bottom inlet flow and initial flow field. At time $t = 0.02$ s, the fluid from both jets form a symmetric shape. At the time $t = 0.101$ s, the symmetry begins to break down as the two jets interact with each other. Much later in the solution, at $t = 1.652$ s, Fig. 12 clearly shows there is no symmetry and the jets appear to overlap one another; the O_2 begins to mix more uniformly throughout the domain. This evolution process in asymmetry has been observed by experiment [38]. Although quantitative profiles are not available from experiment for detailed comparison, the numerical predictions at various times capture the experimental structure fairly well.

6. Conclusions and future work

In this study, we have verified and validated a fourth-order solution-adaptive finite-volume method to solve the compressible Navier–Stokes equations with multispecies governing strong nonlinear physics on mapped domains. The fourth-order accuracy of the algorithm is verified through a Couette flow, species mass diffusion bubble, and two-dimensional vortex convection and diffusion problem. The thermally perfect, multispecies capability is validated using a one-dimensional shock tube and two-dimensional shock box problem. The verified algorithm is then used to simulate the strong nonlinear shock waves on a ramp and the jet mixing transport process. This study produces a fourth-order finite-volume method solving thermally perfect, compressible, multispecies viscous flows with nonlinear, spatially and temporally varying thermodynamic and transport properties on a mapped grid with AMR. The method is capable of handling flows with non-linearity and discontinuities and treating geometry with efficient mapping techniques. Although the algorithm has been implemented for multiple dimensions, the present study focused on the validation in two-dimensional configurations. As a next step, we will perform three-dimensional configurations. Subsequently, we will be able to study the strongly nonlinear combustion processes by using this high-order and high-performance numerical framework.

Acknowledgments

This work was supported by the Office of Advanced Scientific Computing Research of the U.S. Department of Energy (Award number DE-EE0006086), and the National Science Foundation (Award number CCF-1422725).

References

- [1] Pope SB. Computations of turbulent combustion: progress and challenges. *Proc Combust Inst* 1990;591–612.
- [2] Poinot T, Candel S, Troune A. Applications of direct numerical simulation to premixed turbulent combustion. *Prog Energy Combust Sci* 1995;21:531–76.
- [3] Pember RB, Howell LH, Bell JB, Colella P, Crutchfield WY, Fiveland WA, et al. An adaptive projection method for unsteady, low-Mach number combustion. *Combust Sci Technol* 1998;140:123–68.
- [4] Vervisch L, Poinot T. Direct numerical simulation of non-premixed turbulent flames. *Annu Rev Fluid Mech* 1998;30:655–91.
- [5] Day M, Bell J. Numerical simulation of laminar reacting flows with complex chemistry. *Combust Theory Model* 2000;4:535–56.
- [6] Henshaw WD, Schwendeman DW. An adaptive numerical scheme for high-speed reactive flow on overlapping grids. *J Comput Phys* 2003;191:420–47.
- [7] Westbrook CK, Mizobuchi Y, Poinot TJ, Smith PJ, Warantz J. Computational combustion. *Proc Combust Inst* 2005;30(1):125–57.
- [8] Henshaw WD, Schwendeman DW. Moving overlapping grids with adaptive mesh refinement for high-speed reactive and non-reactive flow. *J Comput Phys* 2006;216:744–79.
- [9] Pitsch H. Large-eddy simulation of turbulent combustion. *Annu Rev Fluid Mech* 2006;38:453–82.
- [10] Gao X. A parallel solution-adaptive method for turbulent non-premixed combustions flows. University of Toronto; 2008. Ph.D. thesis.
- [11] Chen J, Choudhary A, de Supinski B, DeVries M, Hawkes E, Klasky S, et al. Terascale direct numerical simulations of turbulent combustion using S3D. *Comput Sci Disc* 2009;2(1).
- [12] Dube A, Antypas K, Ganapathy M, Reid L, Riley K, Sheeler D, et al. Extensible component based architecture for flash, a massively parallel, multiphysics simulation code. *Parallel Comput* 2009;35:512–22.
- [13] Gao X, Groth CPT. A parallel solution-adaptive method for three-dimensional turbulent non-premixed combustions flows. *J Comput Phys* 2010;229:3250–75.
- [14] Wangard W, Dandy D, Miller B. A numerically stable method for integration of the multi-component species diffusion equations. *J Comput Phys* 2001;174:460–72.
- [15] Oran E, Boris J. Numerical simulation of reactive flows. Cambridge University Press; Cambridge; 2005.
- [16] Mazumder S. Critical assessment of the stability and convergence of the equations of multi-component diffusion. *J Comput Phys* 2006;212(2):383–92.
- [17] Kumar A, Mazumder S. Coupled solution of the species conservation equations using unstructured finite-volume method. *Int J Numer Methods Fluids* 2010;64(4):409–42.
- [18] Hydrodynamics adaptive mesh refinement simulation. 2017. URL <https://fpal.stanford.edu/hamers>.
- [19] Parallel implicit adaptive mesh refinement schemes for physically complex flows having disparate scales. 2017. <http://arrow.utias.utoronto.ca/~groth/Research.html>.
- [20] Gao X, Owen LD, Guzik SM. A high-order finite-volume method for combustion. AIAA 2016-1808. 54th AIAA Aerospace Sciences Meeting; 2016.
- [21] Anderson JD. Modern compressible flow with historical perspective. New York: McGraw-Hill; 1990.
- [22] Gordon AS, Li SC, Libby PA, Williams FA. Influence of initial velocity distributions on the height of methane-air nonpremixed flames. *Combust Sci Technol* 1994;100:395–9.
- [23] McBride BJ, Gordon S. Computer program for calculation of complex chemical equilibrium compositions and applications II. Users manual and program description. Reference Publication 1311. NASA; 1996.
- [24] Chase MW. NIST-JANAF thermochemical tables. *J. Phys. Chem. Ref. Data*, 9. 4 ed. American Institution of Physics; 1998.
- [25] Mathur S, Tondon PK, Saxena SC. Thermal conductivity of binary, ternary and quaternary mixtures of rare gases. *Mol Phys* 1967;12(6):569–79.
- [26] Lambert J. Numerical methods for ordinary differential systems. New York: John Wiley & Sons; 1991.
- [27] Guzik SM, Gao X, Owen LD, McCorquodale P, Colella P. A freestream-preserving fourth-order finite-volume method in mapped coordinates with adaptive-mesh refinement. *Comput Fluids* 2015;123:202–17.

- [28] Gao X, Owen LD, Guzik SMJ. A parallel adaptive numerical method with generalized curvilinear coordinate transformation for compressible Navier-Stokes equations. *Int J Numer Meth Fluids* 2016;82:664–88.
- [29] Guzik SM, McCorquodale P, Colella P. A freestream-preserving high-order finite-volume method for mapped grids with adaptive-mesh refinement. 50th AIAA aerospace sciences meeting, AIAA 2012-0574. AIAA; 2012. <https://doi.org/10.2514/6.2012-574>.
- [30] Owen LD, Guzik SM, Gao X. Fourth-order viscous operator on mapped grids. 54th AIAA aerospace sciences meeting, AIAA 2016-0604. AIAA SciTech Forum; 2016. <https://doi.org/10.2514/6.2016-0604>.
- [31] Adams M, Colella P, Graves DT, Johnson JN, Johansen HS, Keen ND, et al. Chombo software package for AMR applications - design document Technical Report LBNL-6616E. Lawrence Berkeley National Laboratory; 2014.
- [32] Guzik SM, Gao X, Olschanowsky C. A high-performance finite-volume algorithm for solving partial differential equations governing compressible viscous flows on structured grids. *Comput Math Appl* 2016;72:2098–118.
- [33] Berger MJ, Colella P. Local adaptive mesh refinement for shock hydrodynamics. *J Comput Phys* 1989;82(1):64–84.
- [34] Colella P, Dorr MR, Hittinger JAF, Martin DF. High-order finite-volume methods in mapped coordinates. *J Comput Phys* 2011;230:2952–76.
- [35] Gao X, Groth CPT. Parallel adaptive mesh refinement scheme for three-dimensional turbulent non-premixed combustion. 46th AIAA aerospace sciences meeting, AIAA 2008-1017; 2008.
- [36] Yee HC, Sandham ND, Djomehri M. Low-dissipative high-order shock-capturing methods using characteristic-based filters. *J Comput Phys* 1999;150(1):199–238.
- [37] Ben-Dor G, Glass II. Domains and boundaries of non-stationary oblique shock-waves reflections. 2. Monatomic gas. *J Fluid Mech* 1980;94:735–56.
- [38] Tryner J, An Q, Mohr J, Steinberg A, Yalin AP, Marchese AJ. High-speed OH* chemiluminescence, OH PLIF, and acetone PLIF imaging of an inverse non-premixed cross-flow flame. In: Proceedings of the western states section of the combustion institute spring 2016 meeting. WSSCI; 2016.